

www.acsanm.org Article

Conductive Conjugated Polymer Nanocapacitors for Localized Electrical Neurostimulation

Manuel E. Martinez-Cartagena, Nicolas E. Muzzio, Rohini Thevi Guntnur, Vanessa Fisher, Skanda Hebbale, Tina Rodgers, Jorge Romero-Garcia, and Gabriela Romero*



Cite This: https://doi.org/10.1021/acsanm.2c03152



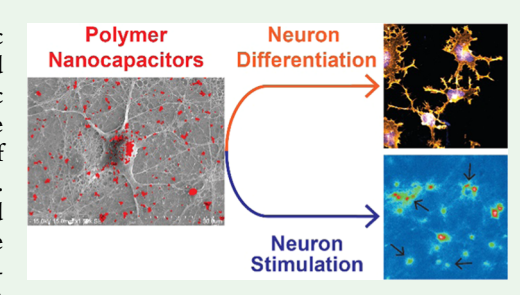
ACCESS I

III Metrics & More

Article Recommendations

s) Supporting Information

ABSTRACT: Noninvasive manipulation of cell signaling is critical in basic neuroscience research and in developing therapies for neurological disorders and tissue engineering and regenerative medicine approaches. In this work, biomimetic synthesized conductive copolymer 3,4-ethylenedioxythiophene (EDOT)-Pyrrole nanoparticles (RB02 NPs) were used for wireless and localized stimulation of neurons. ¹H nuclear magnetic resonance was used to monitor the polymerization. RB02 NPs were characterized by Raman spectroscopy, Fourier transform infrared spectroscopy, and dynamic light scattering. The electrochemical properties were characterized by galvanostatic charge—discharge, voltammetry, and electrochemical impedance spectroscopy. For electrical stimulation of neurons, RB02



NPs were charged by applying 1 V to a NP suspension using platinum electrodes. The effect of NPs on ND7/23 neuron hybrid cell line viability was assessed by live/dead staining using flow cytometry. ND7/23 differentiation was evaluated by cell cytoskeleton staining and quantification of morphological parameters such as the dendrite number and length. Primary cortex neuron stimulation was studied by calcium ion influx detectable through the dynamic fluorescence changes of Fluo-4. RB02 NPs presented no toxicity toward ND7/23 cells. Furthermore, charged NPs enhanced cell differentiation at short times after addition (<6 h). Charged RB02 NPs largely increased the cortex neuronal activity. Altogether, biocompatible copolymer EDOT-Pyrrole nanoparticles present great potential for remote control of neural activities.

KEYWORDS: wireless stimulation, neuronal differentiation, biomimetic synthesis, conductive copolymer, drug-free neurostimulation

1. INTRODUCTION

Noninvasive modulation of neuronal functions is critical for basic neuroscience research and to the development of therapies for neurological disorders and psychiatric conditions, such as Parkinson's disease or depression. Different techniques for drugfree selective and deep stimulation of the nervous system include transcranial magnetic stimulation (TMS), transcranial direct current stimulation (tDCS),² deep brain stimulation (DBS),³ and optogenetics.⁴ These techniques present major drawbacks such as low spatial resolution (about 1 cm) and limited target depth for TMS and tDCS; the requirement of a highly invasive neurosurgical operation to implant the electrodes for DBS and concomitant inflammation and gliosis; and low penetration of visible light through tissues in optogenetic approaches. Recently, transcranial focused ultrasound stimulation (tFUS) has appeared as a promising candidate due to its high spatial resolution (about 1 mm) and long penetration depth.8 Nanotechnology advances are enabling new neuromodulation modalities with deeper penetration, less invasiveness, improved biointerfaces, and higher spatiotemporal precision. Wireless neuronal stimulation has recently been achieved using nanotechnology approaches like magnetomechanical actuation by magnetic discs, ^{10,11} magnetothermal transduction by magnetic nanoparticles, ^{12,13} chemomagnetic approaches, ^{14,15} photothermal polymeric nanotransducers, ¹⁶ electric field generation using piezoelectric nanomaterials, ¹⁷ and photovoltaic effects from conjugated conductive polymers ¹⁸ or magnetoelectric materials. ^{19,20}

In this vein, conjugated conductive polymers are receiving increasing attention due to their electrical and ionic conductivity, which make them ideal for neuronal stimulation. However, traditional chemical polymerizations may require toxic starting materials or generate toxic side products that hinder their use in the interface with living cells. The use of enzymes as green catalysts allows obtaining of macromolecules with a controlled structure and free of toxic products, similarly as in in vivo enzymatic polymerizations. Though enzymes show some drawbacks like weak stability under low pH and organic solvents, several research groups have developed biomimetic synthesis to overcome these limitations. Biomimetic synthesis uses small molecules or nanoparticles that resemble

Received: July 21, 2022 Accepted: August 4, 2022



ACS Applied Nano Materials www.acsanm.org Article

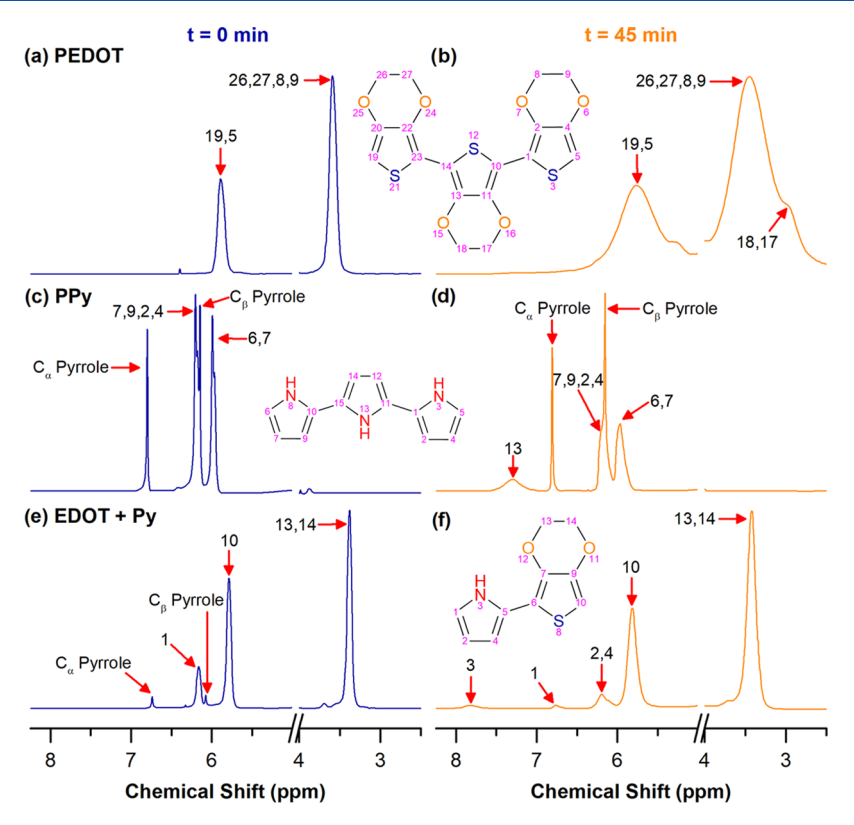


Figure 1. ¹H NMR spectra obtained in D₂O from the polymerization reaction at times 0 min (a, c, e) and 45 min (b, d, f) for PEDOT (a, b), PPy (c, d), and EDOT-Py (e, f). Red arrows indicate the possible proton assignation of chemical shift, α and β protons of the pyrrole ring are denoted as C_α and C_β. Chemical structures contain the associated numeral protons in the ring.

the active site of oxidoreductases, allowing the polymerization of electrically conductive and conjugated polymers. 23,24 The synthesis of conjugated semiconductor polymers (CSP) through biomimetic catalysis has generated great interest in terms of its feasibility to generate new structures using lowenvironmental-impact chemicals and reusable catalysts. Though poly(3,4-ethylenedioxythiophene) (PEDOT) and polypyrrole (PPy) precursor monomers are accessible and inexpensive, ²⁵ their copolymers remain barely studied for application in neuroengineering. 26,27 Several reports have shown the unique properties of conjugated conductive copolymers such as enhanced electrical conductivity and good electrochemical stability and response.²⁸⁻³⁰ Recently, Martinez-Cartagena et al. reported the fabrication of electrocardiogram (ECG) electrodes by the electrophoretic deposition of the 3.4ethylenedioxythiophene (EDOT)-Pyrrole copolymer biomimetically synthesized using hematin as the catalyst.³¹ The electrodes displayed good electrical and electrochemical properties comparable to commercial ECG electrodes. Moreover, Martinez-Cartagena et al. also recently reported the biomimetic synthesis of EDOT-Pyrrole and EDOT-Aniline copolymers, achieving remarkable electrical conductivity and stability in suspension.³² A later publication showed that codoping with ptoluenesulfonic acid and PSS produces highly stable nanoparticle suspensions.

Here, we report the biomimetic synthesis of EDOT-Pyrrole nanoparticles using hematin as the catalyst and their use in neuronal differentiation and neurostimulation. Polymerization of PEDOT, PPy, and EDOT-Py was followed by ¹H nuclear magnetic resonance (NMR). The nanoparticles obtained using a mole fraction of EDOT of 0.9 in the EDOT-Pyrrole copolymer, hereinafter called RB02 NPs, presented accurate electrical

conductivity, suspension stability, and charge storage capacity. In comparison, the NPs obtained using a mole fraction of EDOT of 0.7 and 0.5 presented a diminished electrical conduction.³² RB02 NPs were characterized by dynamic light scattering (DLS), scanning electron microscopy (SEM), Fourier transform infrared spectroscopy (FTIR), and Raman spectroscopy. Further electrochemical characterization was performed by cyclic voltammetry, electrochemical impedance spectroscopy, and galvanostatic charge-discharge measurements. The NPs displayed a pseudocapacitive behavior and large specific capacitance, allowing their use as nanocapacitors by charging them through electrical current exposure, obtaining C-RB02 NPs. ND7/23 cells, a hybrid cell line derived after fusion of primary neonatal rat dorsal root ganglion neurons with mouse neuroblastoma, 33 and primary rat cortical neurons were used for studying the effects of RB02 and C-RB02 NPs on neuronal differentiation and stimulation, respectively. Exposure to C-RB02 NPs enhanced cell differentiation at short times and largely increased the cortex neuronal activity. The adsorption of RB02 NPs on a planar surface was studied by quartz-crystal microbalance with the dissipation monitoring technique (QCM-D) and the obtained values were used to estimate the electrical charge supplied to the cells by C-RB02 NPs. Altogether, biocompatible semiconducting conjugated copolymer EDOT-Pyrrole nanoparticles present great potential for the wireless control of neural activity.

2. RESULTS AND DISCUSSION

2.1. RB02 NPs Synthesis and Characterization. *2.1.1. Polymerization Monitoring via* ¹*H Nuclear Magnetic Resonance.* NMR is a powerful tool for studying polymerization reactions. However, cross-linked polymers require a solid NMR

ACS Applied Nano Materials

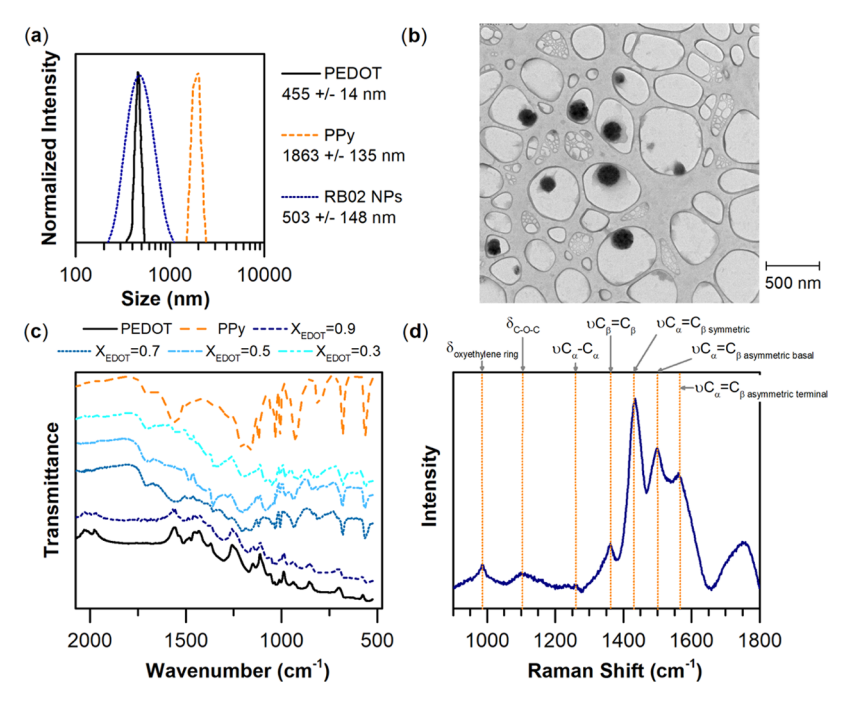


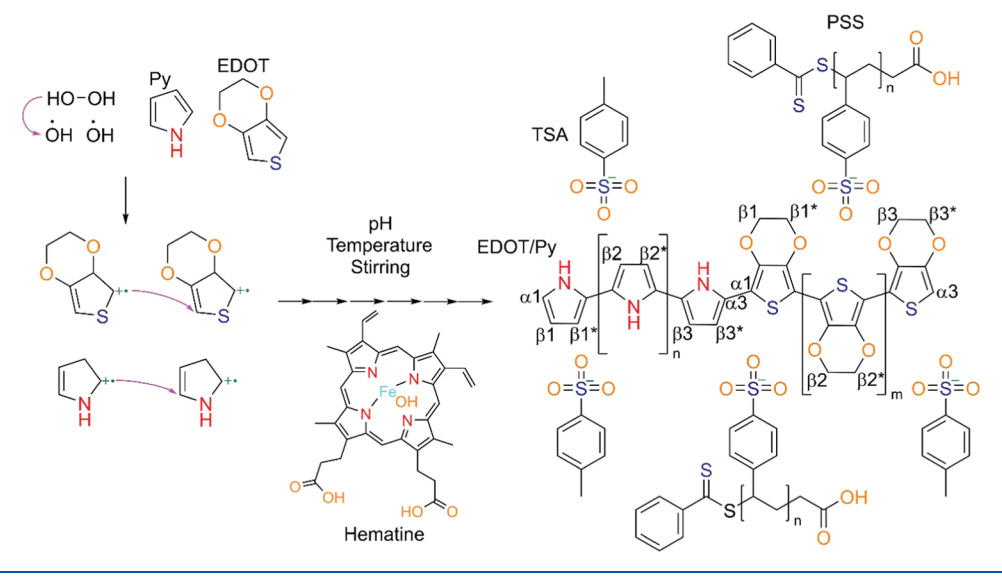
Figure 2. Characterization of RB02 NPs. (a) Hydrodynamic size distribution of PEDOT, PPy, and PEDOT-Py (RB02) NPs. (b) TEM image of RB02 NPs. (c) FTIR spectra of PEDOT and PPy homopolymers and PEDOT-Py copolymers biomimetically synthesized using hematine as the catalyzer. X_{EDOT} represents the EDOT mole fraction in the EDOT-Py copolymer ($X_{\text{EDOT}} = 0.9$ is RB02). (d) Raman spectra of RB02 NPs.

technique due to their insolubility.³⁴ To overcome the limitations that impose the insolubility of PEDOT or PPy polymers or EDOT-Py copolymers, we performed an in situ liquid NMR to monitor the progress of the reaction. The polymerization of PEDOT, PPy, and EDOT-Py using hematin as a catalyst and hydrogen peroxide as an oxidant was monitored using NMR to better understand the mechanism of polymerization (Figure 1). Hematin and then hydrogen peroxide were added to the monomer solution. The reaction was then monitored by NMR spectroscopy. The NMR experiment was conducted by adding D₂O as a solvent and H₂SO₄ as a dopant to a tube containing liquid samples. The tube was then placed in a magnetic field, which caused the nuclei of hydrogen atoms in the sample to process at their characteristic frequency. The frequency of precession depends on the strength of the magnetic field, which can be varied by changing its intensity or orientation. The frequency also depends on the number of protons in each

Figure 1a shows the ¹H NMR spectrum of PEDOT 0 min reaction time, and the spectrum shows two main chemical shifts at 3.6 and 5.9 ppm. The high field signal at 3.6 ppm is assigned to the oxyethylene ring protons undergoing magnetic deprotection of the nucleus. Because of the neighboring oxygens, the second signal at 5.9 ppm shows a different chemical shift with respect to the monomer in CDCl₃ (6.3 ppm), and it has moved upfield and has broadened respect to CDCl₃ probably due to solvent effects (Figure S1). H₂O signal was detected at 4.7 ppm in all samples, probably due to water from the hydrogen peroxide (data not shown). After 45 min of reaction (Figure 1b), it is observed that the signals widen and decrease in intensity, and this is typical in polymeric chains.³⁵ Moreover, a second system appears with signals at 5.27 and 2.98 ppm, which can be attributed to oligomers of higher molecular weight, indicating a change in the chemical environment of molecular structures. In the case of the PPy reaction (Figure 1c), two fine signals are observed at time zero at 6.16 and 6.8 ppm, which are attributed to β and α protons

of the ring, respectively. Two broad signals are shown at 6 and 6.2 ppm (protons in the β position of the ring) and are attributed to the formation of a new aromatic system, which is in agreement with the formation of oligomers in the first second of reaction. After 45 min of reaction (Figure 1d), these signals become broader and more intense, which corresponds to polymer chain growth.³⁶ The chemical shift upfield is associated with the effects of magnetic protection by the chemical environment. Finally, a peak can be identified at 7.3 ppm, which is attributed to the proton of the heteronucleus (N–H). Figure 1e shows the NMR spectrum at time zero of the EDOT-Py copolymerization reaction. Two signals are observed, at 3.4 and 5.8 ppm, which are associated with the EDOT ring, while the small peaks at 6.1 and 6.75 ppm are attributed to the ring of the monomeric pyrrole. The signal at 6.16 ppm is attributed to the β proton of the pyrrole ring of the copolymer in formation. In general, small displacements are observed in the high field of all of the signals, indicating a different chemical environment, maybe corresponding to the interactions between the monomers and the solvent. After 45 min of reaction (Figure 1f), a small peak is observed at 6.77 ppm, which, judging by its intensity and width, could correspond to terminal α protons of the pyrrole in the copolymer. This signal was not observed in the case of the PPy spectrum. The small signals at 6.1 and 6.2 ppm are assigned to the β protons of the pyrrole ring: one corresponds to terminal segments and another to intermediate protons of the copolymer chain that experiences a different chemical environment. The shift of the signal at 6 ppm of the PPy homopolymer to 6.1 ppm in the copolymer can be interpreted as magnetic deprotection of the β protons of the pyrrole ring as an effect generated by neighboring EDOT rings. Likewise, the singlet that moves from 7.3 to 7.8 ppm indicates that the proton of the heteronucleus suffers greater magnetic deprotection, most likely due to the surrounding thiophenic rings. These two changes in the position of the singlets of both the β protons and the protons attached to the N of the pyrrole ring offer strong indications of the formation

Scheme 1. Biomimetic Synthesis of EDOT/Py NPs



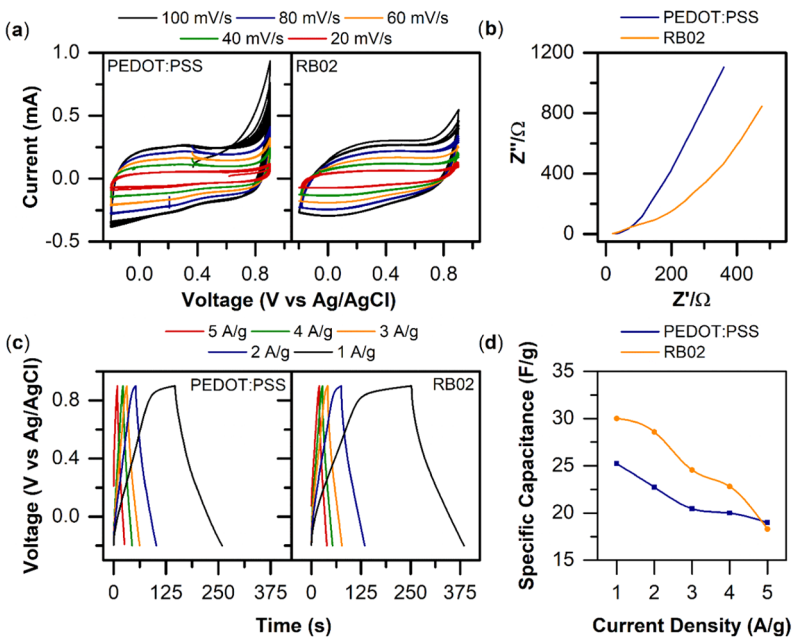


Figure 3. Electrochemical characterization: (a) cyclic voltammetry, (b) electrochemical impedance spectroscopy, and (c) galvanostatic charge—discharge measurements of PEDOT:PSS and RB02 ink drop-cast on a glassy carbon electrode. (d) Specific capacitance vs current density calculated from panel (c).

of the EDOT-Py copolymer. In general, real-time monitoring of EDOT-Py polymerization by NMR offers a consistent and complementary basis to confirm the formation of copolymers, and this contributes as a novel strategy for in situ monitoring the polymerization reaction, considering that the cross-link side reactions eventually produce insoluble nanoparticles, which are not possible to analyze through the liquid NMR technique.

2.1.2. Chemical Characterization. First, the size and morphology of RB02 NPs were characterized. DLS measurement of PEDOT homopolymers presented a narrow size distribution with a mean of 455 nm, and PPy homopolymers presented a broader distribution with a peak at 1863 nm (Figure 2a). RB02 copolymers presented a distribution broader than PEDOT homopolymers and a peak at 503 nm. The size of the dehydrated RB02 NPs observed by transmission electron

microscopy (TEM), though smaller, was in a similar range to the hydrodynamic size found in DLS measurements (black quasi-circular structures in Figure 2b). Additional information of DLS measurements and TEM of RB02 NPs charged at 1 V and 1 A for 30 s (C-RB02 NPs) is shown in Figure S2. As the chemistry of the NPs has not been modified, the exposure of RB02 NPs to the electric field does not significantly affect the size, ζ -potential, and morphology of the NPs.

Chemical characterization of the copolymer was conducted by FTIR and Raman Spectroscopy. The FITR spectrum bands identified for each copolymer EDOT-Pyrrole show coincidence with some bands obtained for its homopolymers (PEDOT and PPy), which corroborates the presence of both chemical structures in the copolymer skeleton, with more resemblance to one or the other depending on the EDOT molar fraction of the copolymer (Figure 2c). Table S1 summarizes the main bands identified in the different copolymers and homopolymers analyzed. RB02 FTIR spectrum shows bands from its homopolymers, in agreement with that previously reported. The Raman spectra of RB02 NPs exhibits two peaks around 1420 and 1500 cm⁻¹, which are associated with symmetric and asymmetric α - β stretching of the thiophene ring (Figure 2d and Scheme 1), and the sharping of the signals between 1500 and 1550 cm⁻¹ indicates conjugation of the segments of polypyrrole. As expected, RB02 NPs appear to show spectral characteristics closer to PEDOT than to PPy. In our previous publication, it is possible to find additional details related to FTIR and Raman studies of EDOT/Py copolymers at different molar ratios. 32

2.1.3. Electrochemical Properties. Cyclic voltammetry (CV) was performed to elucidate the electrochemical behavior of RB02 NPs and to compare it with PEDOT:poly(styrene sulfonate) (PSS), which is one of the most investigated conductive copolymers in the bioelectronics field.³⁹ Specifically, CV developed in a three-electrode configuration is useful in the study of pseudocapacitive contributions inherent to the electrode material. This is the most appropriate technique to investigate any contribution of faradic origin present in the system.²⁸ Figure 3a shows the voltammograms obtained for PEDOT:PSS and RB02 NPs at 100 mV s⁻¹ and a working window of -0.2 to 0.9 V. The graphs show quasi-rectangular shapes that can be attributed to the pseudocapacitive behavior of the materials. The voltammograms do not exhibit evident redox couples, though it is known that there are redox processes associated with protonation and deprotonation of the backbone chain heteroatoms. An ideal electrochemical double layer capacitor (EDLC) generates cyclic voltammograms with a perfect rectangular shape, the presence of Faradic reactions leads to the existence of capacitive peaks that generate the distortion of the rectangular shape toward a quasi-rectangular or completely irregular shape. 40 The discrepancy of the 90° angle concerning the abscissa is governed by the intrinsic resistance of the system. Both PEDOT:PSS and RB02 NPs presented similar trends in electrochemical impedance spectroscopy (Figure 3b) that shows a low charge-transfer resistance between the electrode surface and the solution. Figure 3b shows the Nyquist curves for RB02 and PEDOT, which were obtained in the frequency range from 100 MHz to 100 kHz with an amplitude of 10 mV alternating voltage under conditions of potential of open circuit (E_{oc}) . An impedance spectrum can typically be divided into three regions: high, mid, and low frequencies. The increase in the resistance of the interface with the electrolyte solution and electrode (Ω) shifts the origin of the curves in the Z' axis. The intersection of the curve with the X axis at high frequencies represents the internal resistance of the system or equivalent series resistance (ESR), sum of the resistance of the electrolyte, intrinsic resistance of the active material, and the resistance of the interface between the active material and the collector. These resistances condition the speed of loading and unloading. 41 A good approximation of the ESR can be obtained by reading the initial value of Z' in the Nyquist diagram, which is 20.5 Ω for RB02 and 21.7 Ω for PEDOT. These resistor values are very close, so it can be concluded that the rate of charge transfer is very similar in both materials. Both curves are similar and present two well-defined parts, a section at high frequencies close to 45°, and another at low frequencies ~90°, known as Warbug's tail.⁴² This is the impedance involved in the transfer of ionic current to an electrode by a faradic process and it is a

measure of the ion diffusion rate, which varies inversely with the square root of the frequency. According to the Nyquist diagram of RB02 and PEDOT (Figure 3b), it can be inferred that the diffusion properties of the ions are strongly influenced by the nanostructural characteristics of the material. The low-frequency region exhibits a finite straight line that it extends to high values of Z'' with an angle of $\sim 90^\circ$, which indicates high ionic mobility. Specifically, both the copolymer and PEDOT particles showed very similar trends in the electrochemical impedance spectroscopy (EIS) analysis, which indicates that the copolymer, in addition to having a higher specific capacitance, also shows little resistance to charge transfer between the electrode surface and the solution, the fact that is favorable for efficient electrical discharge in the cell culture bed.

The increments of discharge times (Figure 3c) involve chargetransfer and ionic migration processes and are directly proportional to the increment of material capacitance (Figure 3d). RB02 NPs present larger specific capacitance than PEDOT:PSS. Applying a constant current to the electrode causes the electroactive species to be oxidized/reduced at a constant rate. The electrode potential varies according to the time in which the concentration of the reactants to products modifies the surface of the electrode. 44 Once the charge-transfer and mass transfer processes have started through the electrode, each material takes different times until the electroactive surface has accepted all of the charge that it is capable to store at a constant current.⁴⁵ The increase in discharge time is directly proportional to the increase in the capacitance of the material. RB02 NPs present longer discharge times than PEDOT. This phenomenon has been attributed by different authors to the increase in surface area, decrease in the intrinsic resistance of the material, ordered nanomorphology, and a homogeneous chemical structure throughout the electroactive polymer chains.45-47

The discharge branch time is universally accepted for calculating the specific capacitance of materials, which is calculated according to eq 1 in the Section 4. Figure 3d shows the specific capacitances (C_s) obtained for materials at different current densities. In general, the discharge time increases with decreasing current. At lower currents, the ions slowly diffuse within the electrode, resulting in greater available surface area and therefore greater C_s . On the contrary, with higher current density, the C_s is reduced due to the ionic diffusion limited to the interior of the electrode and governed by the available surface area at the interface. RB02 NPs showed higher specific capacitance, which can be related to the larger surface area as well as faster electronic transfer between the solution and the material.

The higher C_s value of the copolymer is related to the increase in the speed of the electronic and diffusion transfer phenomena due to nanomorphological and structural qualities that favor it, and it also maintains high values of C_s even at high current densities. This indicates that the ionic diffusion rate is not significantly impacted by increasing current density, which is explained by the presence of short ion migration routes and a large available surface area that allows an increase of the electrolyte—electrode interface substantially. The RB02 copolymer was chosen to carry out the biological tests because it presents conduction and capacitance characteristics superior to PEDOT:PSS. Moreover, it shows good balance through ζ -potential, size, and electrochemical performance compared with EDOT 0.7 and 0.5 molar fractions. However, studying the

ACS Applied Nano Materials

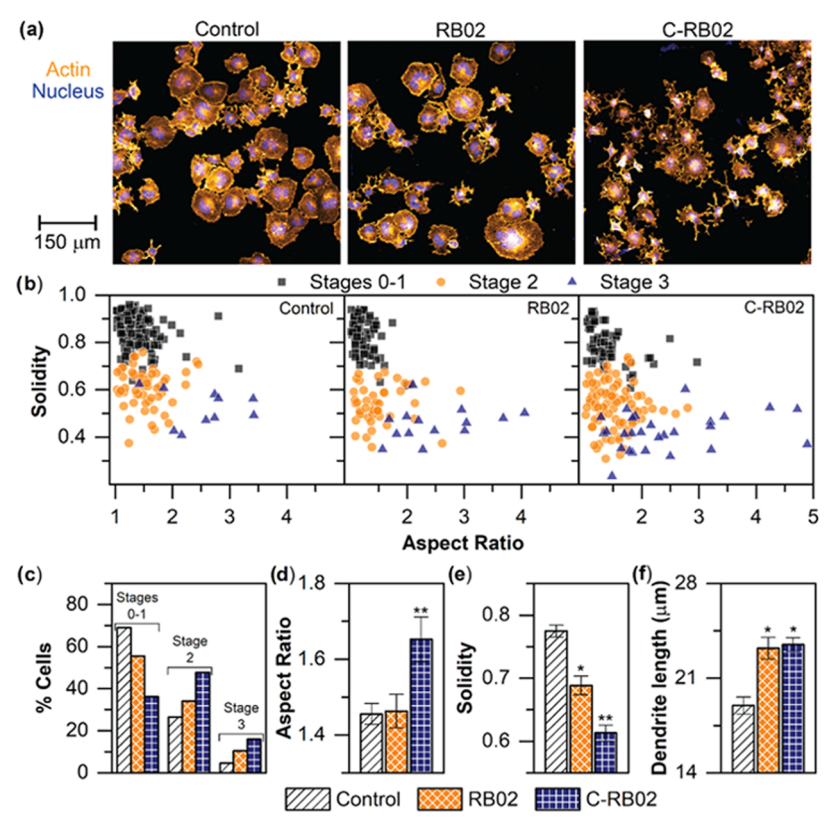


Figure 4. Differentiation of ND7/23 cells 3 h after the addition of β-nerve growth factor (β-NGF), cyclic adenosine monophosphate (cAMP)-supplemented media, and RB02 or charged RB02 NPs. (a) Confocal images of ND7/23 cells (orange, actin cytoskeleton; blue, cell nucleus). (b) Solidity vs aspect ratio scatter plots. Each symbol represents a cell (n is 219, 135, and 182 for control, RB02, and C-RB02 conditions, respectively). (c) Percentage of cells that exhibited stages 0–1, 2, and 3 morphologies when cultured under different conditions. Average (d) aspect ratio, (e) solidity, and (f) dendrite length. The standard error is included. *Indicates statistically significant differences with respect to the control and **indicates statistically significant differences with respect to both control and RB02 condition (one-way ANOVA, followed by Fisher's LSD test, p value <0.05).

biological effect of NPs synthesized with different molar ratios of EDOT and Py is of our interest for future work.

2.2. Cell Stimulation. 2.2.1. DRG-Like Cell Growth and Differentiation. The live/dead assay showed no toxicity of RB02 NPs added to ND7/23 cells for 48 h (viability above 98%, Figure S3). The addition of RB02 and C-RB02 NPs to the cells in differentiation media caused visible effects on the cell morphology (Figure 4a) and consequently cell differentiation. The changes in the cell morphology during neuronal morphogenesis can be divided into five stages. 50,51 In our experimental conditions, only stages 0-1, 2, and an incipient stage 3 were evident. At short times, initially spherical neurons (stage 0) begin extending circumferential lamellipodia and filopodia (stage 1). Then, lamellipodia protrude and stable filopodia become engorged, forming short neurites (neurite initiation, stage 2). Eventually, one of these neurites elongates at a faster rate and becomes the axon (stage 3). Apart from classifying the cells into stages 0-1, 2, and 3, their aspect ratio and solidity (ratio between the cell area and its convex hull) were evaluated to further study their morphology.⁵² Cells on different stages of differentiation presented different trends in their shape factors. Stage 0-1 cells presented solidity values between 0.7 and 1 and aspect ratio values in the 1-2 range (Figure 4b). Stage 2 cells presented aspect ratios between 1 and 2.5 but solidity values in the 0.4-0.7 range. Finally, cells with an incipient axon (stage 3) had solidity values in the 0.3-0.6 range and could reach aspect ratio values of 4-5. With the presence of RB02 NPs, the percentage of cells in stages 0-1 decreased and the percentage

of cells in stages 2 and 3 increased with respect to cells in the control experiment. This effect was more pronounced on the cells exposed to C-RB02 NPs (Figure 4b,c). Moreover, with the addition of C-RB02 NPs, the cells exhibited statistically significant larger aspect ratio and solidity values with respect to both control cells and those exposed to noncharged RB02 NPs (Figure 4d,e). Both RB02 and C-RB02 NPs caused the cells to exhibit longer dendrites (Figure 4f). The mere addition of conductive RB02 NPs has a significant effect in promoting early ND7/23 differentiation, and this effect can be enhanced by charging the NPs before administration. Conductive scaffolds have been shown to promote electroactive cell growth, function, and differentiation, even in the absence of external electrical stimulation.^{53,54} Polymers and nanoparticles with electroconductive properties are promising candidates for neuron stimulation and nervous tissue regeneration. 55,56 However, they are mostly used as constituents of scaffolds, and little is known about their effect when they are directly delivered to cells or as coatings. In situ electrochemical polymerization of conductive PEDOT around living neurons has been performed to generate an electroconductive environment for cells.⁵⁷ Though PEDOT can use the cell membrane as a scaffold for polymerization to obtain an intimate electrode-cell interface, considerable cell damage can be induced depending on the current density. 58 Kim et al. demonstrated that direct delivery of polyaniline and gold nanoparticle nanocomposites followed by electrical stimulation can induce neurogenesis. 59

ACS Applied Nano Materials

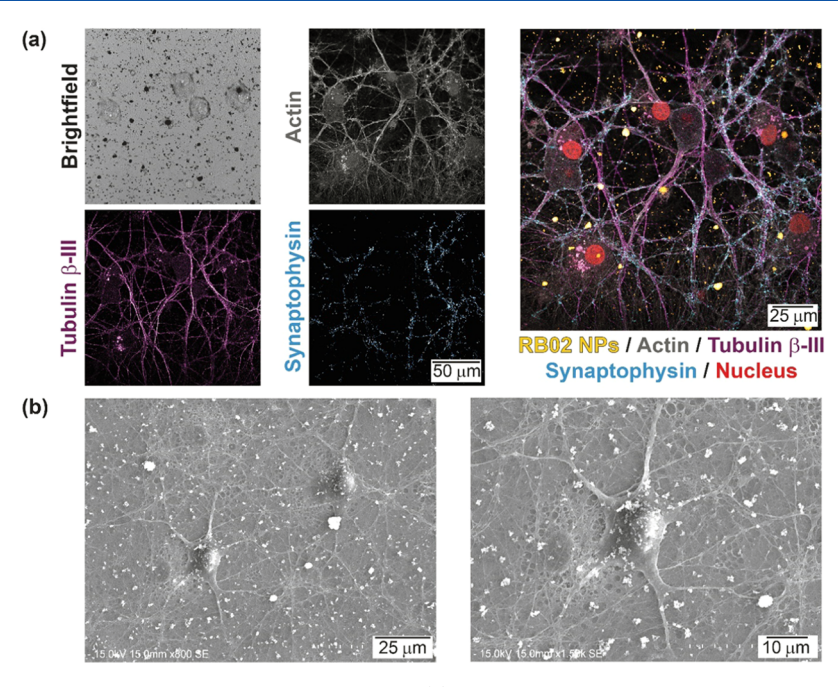


Figure 5. RB02 NP colocalization within primary cortical neural networks. (a) Confocal images of cortical neurons. Cell cytoskeleton microtubules are stained with anti-tubulin β -III (magenta); presynaptic vesicles labeled with a synaptophysin antibody (cyan); actin cytoskeleton is labeled with phalloidin (gray); nuclei counterstaining was performed with DAPI (red); RB02 NPs were imaged in bright field (black dots) and the color was inverted in the merged image (orange). (b) SEM images of cortical neural networks exposed to RB02 NPs (white dots and clusters).

2.2.2. Cortical Cell Stimulation. Confocal microscopy and scanning electron microscopy were performed to study the cell–nanoparticle interface. Figure 5a shows a representative confocal microscopy image of RB02 NPs within cortical neurons. Figure 5b displays scanning electron microscopy (SEM) images of cortical neurons exposed to RB02 NPs. RB02 NPs were found on the cell membrane of cortical neurons localized either in the cell body or within the axons. NP adsorption on top of the planar surface of the silicon dioxide sensor was studied by the QCM-D technique. The adsorbed masses of NPs were 0.22 ± 0.08 , 0.45 ± 0.08 , and $1.1 \pm 0.15 \ \mu g \ cm^{-2}$ at 10, 180, and 1200 min, respectively (Figure S4).

Intracellular calcium dynamics was studied as a reflection of neuronal activity. Calcium imaging videos were recorded for 90 s at 250 frames per second (Video S1). Calcium images illustrate the increase of intracellular calcium (increase of color intensity) over time associated with neuronal stimulation (Figure 6a). Larger neuron activity can be observed in cortical cells cocultured with C-RB02 NPs (Figure 6b). Significantly higher activity was observed for cortical neurons in the presence of C-RB02 NPs with respect to cells in control conditions and cells exposed to RB02 NPs (Figure 6b). Electrical stimulation using electrodes can induce calcium signaling in cortical neurons, dorsal root ganglions,⁶¹ and even nonexcitable brain cells.⁶² Here, wireless electrical stimulation and intracellular calcium release is achieved by charged NPs. The copolymer nanoparticles act as individual nanocapacitors that deliver charge through the double electrochemical layer on multiple points of the neuronal cell membrane, which locally triggers action potentials. This suggests that the charge retention capacity of nanoparticles in the extracellular medium is efficient to generate punctual discharges at the membrane-particle interface. Though the discharge of these pseudocapacitive NPs is almost instantaneous, the discharge of NPs in suspension is not favored as the pseudocapacitors need to experience a potential difference. This can occur by entering in contact with another

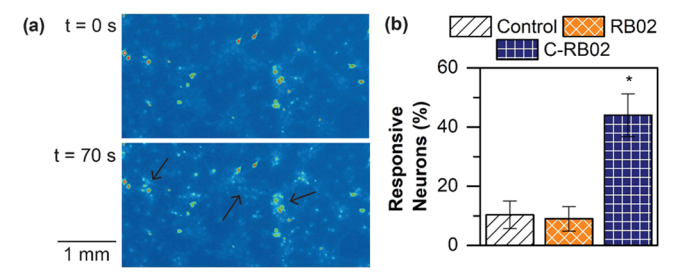


Figure 6. Stimulation of cortical neurons mediated by RB02 NPs. (a) Calcium fluorescence images from a representative video of cortical neurons exposed to C-RB02 NPs at time 0 and 70 s. Areas of increased intracellular calcium concentration are indicated with black arrows. (b) Percentage of responsive neurons determined by dividing the number of neurons that were active at least 0.75 s during the length of the video by the total number of analyzed neurons. *Indicates statistically significant differences with respect to both control and RB02 condition (one-way ANOVA, followed by Fisher's LSD test, *p* value <0.05).

surface such as air, petri dish walls, or the cell membrane. Thus, the discharge kinetics should be governed up to some point by the mass deposition kinetics (Figure S4). It is worth noting that due to hardware and data-size limitations, neuron stimulation videos were recorded for just 90 s, but two or three videos focusing different regions of the petri dish were recorded one after the other upon adding the C-RB02 NPs and the cells remained active during those $6{-}10$ min time period.

Considering that the RBO2 NPs have a specific capacitance of 30 F g⁻¹ by charging them at 1 V and 1 A g⁻¹ for 250 s (Figure 3c,d) and that for cell experiments the NPs were charged through 30 s at 1 V and 1 A, it is possible to estimate the approximated total charge amount delivered in the stimulation experiment (see Supporting Note 1). A mass density of 0.22 μ g cm⁻² of NPs should be adsorbed on top of the cells at 10 min of incubation (the time needed to add the suspension of NPs, focus the cells on the microscope, and take three videos of 90 s). The

charge per cm⁻² in the 10 min electrical stimulation experiment with cortical neurons is ~6.6 μ F or considering that we charged the particles at 1 V, 6.6 μ C. This value is enough current to depolarize electrical responsive cells.⁶³ In vivo experiments using capacitor electrodes implanted in a cat's cortex showed that using 0.8–1 μ C pulses per hour is enough to evoke neuronal activity.⁶⁴

3. CONCLUSIONS

In this work, we developed a soft nanomaterial platform for the wireless stimulation of biological signaling in neurons. Biomimetic synthesized conductive EDOT-Pyrrole copolymers doped with PSS (RB02 NPs) were used to fabricate nanocapacitors. Biomimetic synthesis was utilized to avoid cytotoxicity of the nanomaterials associated with traditional wet chemistry protocols. The biomimetic synthesized RB02 NPs display similar charge-transfer velocity and larger specific capacitance as PEDOT:PSS, a benchmark in electroconductive materials for bioengineering applications. Electroconductive RB02 NPs were shown to enhance ND7/23 differentiation within 3 h of coculturing. The differentiation effect was more pronounced when charged nanoparticles were employed. As anticipated, RB02 NPs showed no toxicity toward ND7/23 cells in our live/dead assays. To our knowledge, this work is among the first reporting the capability of standalone conductive nanoparticles for cell differentiation. Previous investigations using conductive nanoparticles to promote cell differentiation rely on conductive polymeric scaffolds to interface with cells. The nanocapacitor behavior of RB02 NPs was shown to evoke neural activity. Charged RB02 NPs largely increased the neuronal activity in primary rat cortical networks assessed by calcium imaging. Further work will investigate the specific biophysical mechanism that allows localized wireless electrical stimulation and ionic bases for the enhanced neuronal cell differentiation. Overall, the biocompatible RB02 NPs fabricated here have a great potential for the remote control of biological signaling, which is anticipated to contribute in the progress of basic neuroscience research and in developing novel neurological therapies.65

4. EXPERIMENTAL SECTION

- 4.1. Biomimetic Synthesis of Nanoparticles. In our experiments, 1 mL of a 100 mg mL⁻¹ hematine (Sigma-Aldrich) solution in dimethyl sulfoxide (DMSO, Sigma-Aldrich) and 200 mg of 3,4ethylenedioxythiophene (EDOT, Sigma-Aldrich) were added to 20 mL of 1:40 poly(styrene sulfonate) (PSS)/toluene sulfonic acid (TSA) (Sigma-Aldrich) solution pH 2. PSS with a molecular weight of 70 000 g mol^{-1} was obtained by RAFT (sodium p-styrenesulfonate was used as the precursor, Sigma-Aldrich). The emulsion was stabilized for 2 h under magnetic stirring. Then, pyrrole (Py) was added, and constant stirring was maintained at 1000 rpm for 2 h at room temperature. To obtain RB02 NPs, Py was added to maintain a molar fraction of EDOT equal to 0.9 ($X_{\rm EDOT} = 0.9$). Polymerization begins by microdosing 200 μ L of 30% H₂O₂ for 1 min, keeping the system at 0 °C. The temperature and stirring conditions (0 °C, 250 rpm) were sustained for 18 h. Each copolymer was frozen at -25 °C and lyophilized for 24 h, then resuspended in cold acetone, filtered on a 0.25 µm polytetrafluoroethylene (PTFE, Merck) membrane, and multiple acetone washes were running over the product until a colorless filtered liquid was obtained. Finally, the product was dried at 70 °C for 12 h. The synthesis of the homopolymers and copolymers without PSS, doped only with TSA, was carried out keeping the same synthesis conditions described above.
- **4.2.** ¹H Nuclear Magnetic Resonance Spectroscopy. NMR spectra of the solution were obtained on a Brucker Avance III HD Ascend 400 MHz spectrometer with a 5 mm multinuclear cryogenic

probe, with Z-grad. $^1\mathrm{H}$ spectra were acquired with 30° pulses and 1 s hold times.

- **4.3. Dynamic Light Scattering (DLS).** The synthesized materials were dispersed on distilled water (1 mg mL $^{-1}$) and size distribution measurement was carried out by dynamic light scattering with a ζ -sizer Nano S90 equipment, operating a He–Ne laser at 633 nm and 4 mW, with a detection angle of 90°. The diameters of the particles by average intensity and the polydispersity index (PDI) were calculated by cumulative analysis according to the ISO13321 standard. The size distribution by intensity was obtained from function correlation analysis using the general-purpose algorithm included in the instrument software, and the said algorithm is based on nonnegative least-squares fit.
- **4.4. Transmission Electron Miscroscopy (TEM).** Transmission electron microscopy images were taken on a Titan Fei Thermo Fischer instrument with an acceleration voltage of 200 kV. The samples were prepared by immersing lacey-carbon grids in an isopropanol suspension (1 mg mL^{-1}) , allowing them to dry in a vacuum oven for 2 h at 60 °C.
- **4.5. Fourier Transform Infrared Spectroscopy (FTIR).** Fourier transform infrared spectra were acquired using a Thermo Fischer Scientific FTIR Spectrophotometer in the attenuated total reflectance (ATR) mode using a diamond crystal. The nanoparticle powder was placed on the surface of the ATR crystal (KRS-5) and the measurement was carried out by taking an average of 32 scans with a resolution of 4 cm⁻¹ within a range of 400–4000 cm⁻¹.
- **4.6. Raman Spectroscopy.** Raman spectra were acquired on a LabRAM HR Evolution confocal Raman microscope, using a 100× objective, 532 nm laser, 10 accumulations, 20 s acquisition time, and a 400–1800 cm⁻¹ range (ND filter 5%, grating 600 (500 nm)).
- 4.7. Electrochemical Characterization. 4.7.1. Preparation of the Working Electrode (WE). The working electrodes were prepared by dispersing 4 mg of RB02 or PEDOT:PSS in 1 mL of ethanol/water (1:1), using 10 μ L of naphion 0.05 wt % as a binder (Sigma-Aldrich). The mixture was dispersed in an ultrasonic bath for 15 min, obtaining a homogeneous and stable suspension. A volume of 10 μ L of the obtained suspension was deposited (taking extreme care to measure volumes and the correct application on the exposed area of the electrode) on a 3 mm diameter vitreous carbon electrode, completely covering the work area without the existence of interior cavities or external remnants. This is decisive to compare the amount of active material between experiments. Multiple repetitions of the electrode were fabricated for each material to statistically ensure that the measurements were not biased by human error. The electrodes coated with the active material were dried at 60 °C for 60 min. Cyclic voltammetry (CV) was performed on the electrodes prepared according to the previous step using a Biologic SP potentiostat and using a three-electrode cell, where the working electrode (we) corresponds to a 3 mm vitreous carbon electrode coated with the materials to be evaluated, the counter electrode (CE) consists of a platinum wire, and Ag/AgCl was used as a reference electrode (RE). The electrolyte of choice was phosphate-buffered saline (PBS) solution in all tests. Once the electrodes were submerged in the electrolyte, N₂ was bubbled in for 20 min. The operating conditions consisted of a potential window of -0.2 to 0.9 V, and sweep speeds from 5 to 100 mV s^{-1} in 10 cycles.
- 4.7.2. Galvanostatic Charge–Discharge. The galvanostatic charge–discharge test basically consists of a chronopotentiometric experiment. The cell configuration and the electrolyte correspond to the aforementioned. In this measurement, the current was set at 0.2, 1, 2, 3, 4, and 5 A $\rm g^{-1}$ and the potential window was -0.2 to 0.9 V. The specific capacitance reported in this work is derived from this measurement, which is calculated according to eq 1

$$C_{\rm s} = \frac{it}{m\Delta V} \tag{1}$$

where $C_{\rm s}$ is the specific capacitance, i is the current used, t is the discharge time, m is the mass of the pseudocapacitor material, and ΔV is the potential window used. The calculation of power density and energy density was carried out using eq 2

$$E = \frac{1}{8}CV^2 \tag{2}$$

In the case of a three-electrode cell, a correction must be made that results in division using a factor four times greater.

4.7.3. Electrochemical Impedance Spectroscopy. Electrochemical Impedance spectroscopy was performed respecting the cell and electrolyte configuration described above. Measurements were performed at an alternating voltage amplitude of 10 mV in the frequency range from 100 mHz to 100 kHz against the open-circuit potential ($E_{\rm oc}$).

4.8. Quantification of Nanoparticle Adsorption Using the QCM-D Technique. Adsorption of RB02 nanoparticles on a planar surface was studied using the quartz-crystal microbalance with a dissipation (QCM-D) technique. QCM-D measurements were performed on a QSense Explorer microbalance with a single channel (Biolin Scientific). A 14 mm diameter silicon dioxide-plated quartz crystal with a fundamental frequency of 5 MHz was used as a sensor (QSX 303, Biolin Scientific). The frequency and dissipation were recorded for seven odd overtones (1st-13th). The sensors were cleaned before the experiment according to the procedures recommended by the manufacturer. Briefly, the crystals were exposed to a UV/ozone treatment for 15 min, sonicated for 15 min in 2% w/v solution of sodium dodecyl sulfate (SDS), rinsed thoroughly with Millipore water, air dried, and treated again with UV/ozone for 15 min. Frequency and dissipation values before RB02 NP adsorption were determined in air and verified to be within the acceptable range specified by the manufacturer. Then, the sensors were removed from the QCM-D chamber, placed on top of a parafilm sheet inside a 35 mm petri dish, a 14 mm diameter rubber O-ring placed on top of the sensor and 250 μ L of a 10 μ g mL⁻¹ suspension of nanoparticles in Millipore water added. After 0, 10, 180, and 1200 min, the liquid was carefully removed using a pipette and the sensor was dried in an oven at 37 $^{\circ}$ C. As it is not possible to remove all of the liquid with a pipette tip, time 0 min was used to correct the other times for the adsorption of NPs from the liquid remaining after pipetting. The sensors were placed inside the QCM-D chamber and frequency and dissipation values were determined in air. Each condition was tested at least three times, performing the cleaning process between each replicate.

Changes in frequency (ΔF) and dissipation (ΔD) were calculated by subtracting the frequency and dissipation values after incubation with RB02 NPs by the ones determined before (after cleaning) for that sensor. The adsorbed mass (m) was calculated using Sauerbrey equation (eq 3)

$$m = -C_{\text{QCM}} \frac{\Delta F_n}{n} \tag{3}$$

where $C_{\rm QCM}$ is the mass sensitivity constant of the crystal, which is 17.7 ng cm $^{-2}$ Hz $^{-1}$ for crystals with a fundamental frequency of 5 MHz, and n is the overtone number. The Sauerbrey equation can be applied to model the adsorbed mass of monolayers of discrete particles or nanosized objects, provided that the layer is rigid. In our experiments, the relationship $|\Delta D_n/(\Delta F_n/n)|$ was smaller than 4×10^{-7} Hz $^{-1}$ and the overtone-normalized frequency shift was independent of the overtone order $(\Delta F_n/n \sim {\rm constant})$, fulfilling the conditions to use the Sauerbrey equation. As the measurements were performed in air after drying the samples, we expect the solvated solvent and trapped solvent effect to be minimal, and we assume that the calculated mass is of RB02 NPs. An adsorbed mass of $2.29 \pm 0.06~\mu {\rm g}~{\rm cm}^{-2}$ was obtained for a sample where the 250 $\mu {\rm L}$ of suspension of NPs was dried, close to the expected value of $2.5~\mu {\rm g}~{\rm cm}^{-2}$.

4.9. ND7/23 Cell Culture and Differentiation. ND7/23 cells, mouse neuroblastoma x rat dorsal root ganglion neuron hybrid cell line produced by poly(ethylene glycol) (PEG)-mediated cell fusion, were used for cell differentiation experiments (Sigma, 92090903). Cells were cultured at 37 °C and 5% CO₂ in Dulbecco's modified Eagle's medium (DMEM, 10-014-CV, Corning) supplemented with 10% fetal bovine serum (FBS, 35-010-CV, Corning) and 1% penicillin—streptomycin (15140-122, Gibco), hereinafter, complete DMEM.

ı

For differentiation experiments, cells were seeded on 35 mm collagen-coated glass-bottom dishes (P35GCOL-0-14-C, MatTek) at a concentration of 25 000 cells per dish and cultured for 24 h to allow attachment. After that, the media was replaced by 2 mL of complete DMEM supplemented with 50 ng mL⁻¹ recombinant rat β -nerve growth factor (β -NGF, 556-NG-100/CF, R&D Systems) and 1 mM dibutyryl-cAMP (dbcAMP, S7858, Selleckchem), hereinafter differentiation media, with or without 10 μ g mL⁻¹ of RB02 or charged RB02 (C-RB02) nanoparticles. Twenty micrograms of RB02 NPs was charged in a chamber consisting of platinum electrodes (3 mm apart) with a cap secured to a vial containing 2 mL of differentiation media and connected to a 1 V at 1 A generator. The media was exposed for 30 s to the electric field before being transferred to the dish with cells. Therefore, in this study, instant and wireless electrical stimulation was applied. After media replacement, the cells were incubated for 3 h before fixation. Each condition was performed by tetra plicate.

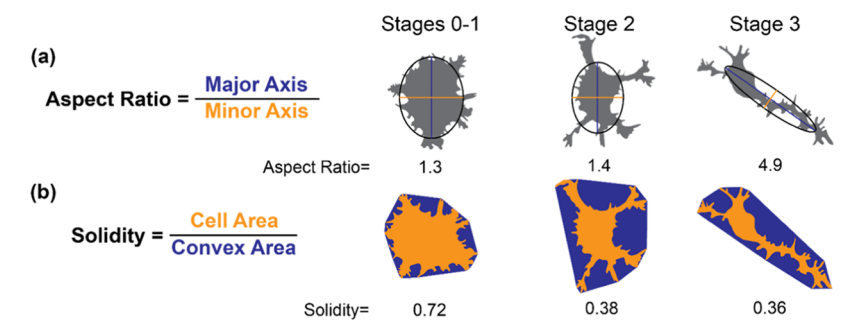
4.10. Live–Dead Assay. To assess the effect of RB02 NPs exposure on cell viability, a live/dead assay was used to quantify live and dead cell populations using flow cytometry. Cells were seeded in a 96-well plate (Greiner) at a concentration of 10^3 cells per well in $200~\mu$ L of complete DMEM. After 24 h, to allow cell attachment, RB02 NPs were added at a concentration of $50-250~\mu$ g mL $^{-1}$. After 24–48 h incubation with RB02 NPs, the medium was aspirated and $50~\mu$ L of TrypLE Express (12604-013, Gibco) was added to detach the cells from the wells. The cells were suspended in $200~\mu$ L of fluorescence-activated cellsorting buffer (FACS buffer) containing 0.8 μ M Calcein (C34852, Invitrogen) and 0.5 μ M Sytox (S34859, Invitrogen) to stain the live and dead cells, respectively. FACS buffer was prepared by mixing $20~\mu$ L of 0.5 M EDTA and $20~\mu$ L of FBS in 20~mL of PBS. The live and dead cell populations were then quantified using flow cytometry (BD Accuri C6 Plus, Becton–Dickinson, Franklin Lakes, NJ).

4.11. Isolation and Maintenance of Primary Rat Cortical Neurons. All experiments in this study were approved by the UTSA Institutional Animal Care and Use Committee (approval no. MURA007). Cortex was extracted from neonatal rats, dissociated, and plated on 35 mm collagen-coated glass-bottom dishes. ^{70,71} Primary neurons were maintained in neurobasal media (21103-049, Gibco) supplemented with 2% B27 (17504-044, Gibco) and 1% Glutamax-I (35050-061 Gibco) at 37 °C and 5% CO₂. Glial inhibition was performed after 3 days with a solution of 5-fluoro-2'-deoxyuridine and uridine (FURD, Sigma-Aldrich). Half of the media was replaced with fresh media every other day.

4.12. Neuron Stimulation Experiments. Cells were labeled prior to stimulation experiments with the calcium indicator Fluo-4 (F10471, Invitrogen) following the manufacturer's protocol. The experiments were performed on healthy cultures between 8 and 12 days after isolation. Culture media was removed from the dishes and replaced with Tyrode buffer with or without RB02 or C-RB02 NPs (10 μ g mL⁻¹). Cells were imaged for 90 s under a stereomicroscope (Leica M205 FCA) equipped with 2× and 5× Plan Apo objectives, and a sCMOS camera (Leica DFC9000).

4.13. Immunohistochemistry and Confocal Imaging. For the fluorescence staining of cell actin cytoskeleton, microtubules, presynaptic vesicles, and cell nucleus, the samples were fixed with 4% paraformaldehyde in PBS. After washing 3 times with washing solution, i.e., PBS containing 0.05% Tween-20 (BP337, Fisher Bioreagents), cells were permeabilized with 0.25% Triton X-100 (T8787, Sigma-Aldrich) for 10 min followed by three washes. Blocking solution, i.e., 1% bovine serum albumin (0332, VWR) in PBS, was applied for 1 h. Anti-tubulin β-III antibody (clone TU-20, Alexa Fluor555 Conjugate, CBL412A5 from Sigma-Aldrich) and mouse monoclonal synaptophysin antibody (Alexa Fluor647 Conjugate, NBP147483AF647 from Novus Biologicals) were diluted to a working concentration in blocking solution, added to the samples, and incubated overnight at 4 °C. Cells were washed 3 times 10 min each, and actin cytoskeleton was stained using Acti-Stain 488 Phalloidin (PHDG1-A, Cytoskeleton). After incubation for 1 h, the cells were washed 3 times and cell nucleus counterstaining was performed by incubating with DAPI for 5 min (90229, Merck Millipore). The samples were washed, and PBS was added to the petri dish before visualization in a Leica TCS SP8 confocal microscope.

Scheme 2. Typical Shapes of Cells on Stages 0-1 (Rounded Cells or Cells Extending Circumferential Lamellipodia and Filopodia, Respectively)a-d



^b(a, b) Schematic representation of aspect ratio and solidity determination, respectively. ^cAspect ratio is calculated as the quotient between the major (blue) and minor (orange) axes of the best fitting ellipse (black) of the cell area (a). ^astage 2 (cells exhibiting multiple minor neurites), and stage 3 (cells presenting one elongated neurite that will become the axon). ^dSolidity is calculated as the ratio between the cell area (orange area) and the convex hull area (blue area + orange area) (b).

Image processing was completed using the open-source software Image] (Fiji) 1.52p (National Institutes of Health).

4.14. Sample Preparation for Scanning Electron Microscopy. Samples were rinsed twice with PBS and fixed with 4% paraformaldehyde in PBS. Cells were gradually dehydrated in a serial change of ethanol in Milli-Q water for 5 min each (0, 5, 10, 25, 35, 50, 65, 75, 90, 100%). Then, 100% ethanol was removed and the samples were exposed to 2:1 and 1:2 solutions of ethanol/hexamethyldisilazane (AAA15139AC, Fisher), 20 min each. Finally, the samples were left with hexamethyldisilazane for 20 min, then it was removed leaving a thin layer covering the cells, and samples were left to dry. The glass bottom was carefully removed from the petri dish. The samples were mounted on aluminum pin stubs using a double-sided carbon tape and gold-coated (PELCO SC-7 Sputter Coater) before imaging in a Hitachi SU1510 scanning electron microscope.

- **4.15.** Quantification of ND7/23 Cell Differentiation. Cell differentiation stages were manually tagged according to their shape. ^{50,51} Cell morphologic parameters were quantified to evaluate differentiation under different conditions. Cell contours were manually traced and analyzed using ImageJ. Aspect ratio and solidity were chosen as shape descriptors to characterize different stages of cell differentiation (Scheme 2). Cell dendrite length was quantified using Neuron] (Image] plugin).
- **4.16. Analysis of Calcium Imaging.** The analysis was performed using ImageJ functions to subtract the background and measure the fluorescence intensity. Time resolution of fluorescence microscopy was insufficient to be interpreted as resolving individual spikes. Instead, it might be taken to show time-integrated levels of neuronal activity. An automated code was generated in MATLAB to analyze the fluorescence intensity traces of neurons in each video. Three different videos containing 300–500 neurons were analyzed for each condition.
- **4.17. Statistical Analysis.** Experiments were performed in triplicate unless otherwise stated. All data were reported as mean \pm standard error unless otherwise stated. One-way analysis of variance (ANOVA) followed by Fisher's least significant difference (LSD) test was performed for means comparison (significance level of 0.05, OriginPro 2016).

ASSOCIATED CONTENT

Supporting Information

The Supporting Information is available free of charge at https://pubs.acs.org/doi/10.1021/acsanm.2c03152.

NMR spectral data; FTIR spectroscopy data, and livedead data (PDF)

Calcium fluorescence imaging videos of primary rat cortical neurons untreated and treated with RB02 or C-RB02 NPs (MP4)

AUTHOR INFORMATION

Corresponding Author

Gabriela Romero – Department of Biomedical Engineering and Chemical Engineering, The University of Texas at San Antonio, San Antonio, Texas 78249, United States;

orcid.org/0000-0001-8081-2946; Email: gabrielaromero.uribe@utsa.edu

Authors

Manuel E. Martinez-Cartagena – Advanced Materials Department, Research Center in Applied Chemistry (CIQA), Saltillo, Coahuila 25294, Mexico

Nicolas E. Muzzio – Department of Biomedical Engineering and Chemical Engineering, The University of Texas at San Antonio, San Antonio, Texas 78249, United States

Rohini Thevi Guntnur — Department of Biomedical Engineering and Chemical Engineering, The University of Texas at San Antonio, San Antonio, Texas 78249, United States

Vanessa Fisher — Department of Biomedical Engineering and Chemical Engineering, The University of Texas at San Antonio, San Antonio, Texas 78249, United States

Skanda Hebbale — Department of Biomedical Engineering and Chemical Engineering, The University of Texas at San Antonio, San Antonio, Texas 78249, United States

Tina Rodgers – Department of Biomedical Engineering and Chemical Engineering, The University of Texas at San Antonio, San Antonio, Texas 78249, United States

Jorge Romero-Garcia — Advanced Materials Department, Research Center in Applied Chemistry (CIQA), Saltillo, Coahuila 25294, Mexico

Complete contact information is available at: https://pubs.acs.org/10.1021/acsanm.2c03152

Author Contributions

The manuscript was written through contributions of all authors. All authors have given approval to the final version of the manuscript. M.E.M.-C. and N.E.M. contributed equally to this work.

Notes

The authors declare no competing financial interest.

ACKNOWLEDGMENTS

This work was partially supported by the National Science Foundation under a CAREER award to G.R. (CBET—2044713). M.E.M.-C. thanks FONCYT for financial support through the projects COAH-2020-C14-B007 and CB2016—287954-Q. This paper is dedicated to the memory of our collaborator J.R.-G., who passed away while preparing this manuscript.

ABBREVIATIONS

EDOT, 3,4-ethylenedioxythiophene NPs, nanoparticles CSP, conjugated semiconductor polymers PPy, polypyrrole PSS, poly(styrene sulfonate) DLS, dynamic light scattering SEM, scanning electron microscopy FTIR, Fourier transform infrared spectroscopy TEM, transmission electron microscopy CV, cyclic voltammetry ESR, equivalent series resistance EIS, electrochemical impedance spectroscopy cAMP, cyclic adenosine monophosphate β -NGF, β -nerve growth factor (DAPI), 4',6-diamidino-2-phenylindole

REFERENCES

- (1) Romero, M. C.; Davare, M.; Armendariz, M.; Janssen, P. Neural effects of transcranial magnetic stimulation at the single-cell level. *Nat. Commun.* **2019**, *10*, No. 2642.
- (2) Chase, H. W.; Boudewyn, M. A.; Carter, C. S.; Phillips, M. L. Transcranial direct current stimulation: a roadmap for research, from mechanism of action to clinical implementation. *Mol. Psychiatry* **2020**, 25, 397–407.
- (3) Lozano, A. M.; Lipsman, N.; Bergman, H.; Brown, P.; Chabardes, S.; Chang, J. W.; Matthews, K.; McIntyre, C. C.; Schlaepfer, T. E.; Schulder, M.; Temel, Y.; Volkmann, J.; Krauss, J. K. Deep brain stimulation: current challenges and future directions. *Nat. Rev. Neurol.* **2019**, *15*, 148–160.
- (4) Chen, S.; Weitemier, A. Z.; Zeng, X.; He, L.; Wang, X.; Tao, Y.; Huang, A. J. Y.; Hashimotodani, Y.; Kano, M.; Iwasaki, H.; Parajuli, L. K.; Okabe, S.; Teh, D. B. L.; All, A. H.; Tsutsui-Kimura, I.; Tanaka, T. F.; Liu, X.; McHugh, T. J. Near-infrared deep brain stimulation via upconversion nanoparticle—mediated optogenetics. *Science* **2018**, 359, 679–684.
- (5) Lee, W.; Kim, H.-C.; Jung, Y.; Chung, Y. A.; Song, I.-U.; Lee, J.-H.; Yoo, S.-S. Transcranial focused ultrasound stimulation of human primary visual cortex. *Sci. Rep.* **2016**, *6*, No. 34026.
- (6) Krauss, J. K.; Lipsman, N.; Aziz, T.; Boutet, A.; Brown, P.; Chang, J. W.; Davidson, B.; Grill, W. M.; Hariz, M. I.; Horn, A.; Schulder, M.; Mammis, A.; Tass, P. A.; Volkmann, J.; Lozano, A. M. Technology of deep brain stimulation: current status and future directions. *Nat. Rev. Neurol.* 2021, 17, 75–87.
- (7) Yu, N.; Huang, L.; Zhou, Y.; Xue, T.; Chen, Z.; Han, G. Near-Infrared-Light Activatable Nanoparticles for Deep-Tissue-Penetrating Wireless Optogenetics. *Adv. Healthcare Mater.* **2019**, 8, No. 1801132.
- (8) Kim, S.; Jo, Y.; Kook, G.; Pasquinelli, C.; Kim, H.; Kim, K.; Hoe, H.-S.; Choe, Y.; Rhim, H.; Thielscher, A.; Kim, J.; Lee, H. J. Transcranial focused ultrasound stimulation with high spatial resolution. *Brain Stimul.* **2021**, *14*, 290–300.
- (9) Yang, X.; McGlynn, E.; Das, R.; Paşca, S. P.; Cui, B.; Heidari, H. Nanotechnology Enables Novel Modalities for Neuromodulation. *Adv. Mater.* **2021**, *33*, No. 2103208.
- (10) Collier, C.; Muzzio, N.; Thevi Guntnur, R.; Gomez, A.; Redondo, C.; Zurbano, R.; Schuller, I. K.; Monton, C.; Morales, R.; Romero, G. Wireless Force-Inducing Neuronal Stimulation Mediated by High

- Magnetic Moment Microdiscs. Adv. Healthcare Mater. 2022, 11, No. 2101826.
- (11) Gregurec, D.; Senko, A. W.; Chuvilin, A.; Reddy, P. D.; Sankararaman, A.; Rosenfeld, D.; Chiang, P.-H.; Garcia, F.; Tafel, I.; Varnavides, G.; Ciocan, E.; Anikeeva, P. Magnetic Vortex Nanodiscs Enable Remote Magnetomechanical Neural Stimulation. *ACS Nano* **2020**. *14*, 8036–8045.
- (12) Hescham, S.-A.; Chiang, P.-H.; Gregurec, D.; Moon, J.; Christiansen, M. G.; Jahanshahi, A.; Liu, H.; Rosenfeld, D.; Pralle, A.; Anikeeva, P.; Temel, Y. Magnetothermal nanoparticle technology alleviates parkinsonian-like symptoms in mice. *Nat. Commun.* **2021**, *12*, No. 5569
- (13) Jiménez, G. L.; Guntnur, T. R.; Guiliani, J.; Romero, G. Enhancing magnetic hyperthermia in ferrite nanoparticles through shape anisotropy and surface hybridization. *AIChE J.* **2021**, *67*, No. e17437.
- (14) Rao, S.; Chen, R.; LaRocca, A. A.; Christiansen, M. G.; Senko, A. W.; Shi, C. H.; Chiang, P.-H.; Varnavides, G.; Xue, J.; Zhou, Y.; Park, S.; Ding, R.; Moon, J.; Feng, G.; Anikeeva, P. Remotely controlled chemomagnetic modulation of targeted neural circuits. *Nat. Nanotechnol.* **2019**, *14*, 967–973.
- (15) Guntnur, R. T.; Muzzio, N.; Gomez, A.; Macias, S.; Galindo, A.; Ponce, A.; Romero, G. On-Demand Chemomagnetic Modulation of Striatal Neurons Facilitated by Hybrid Magnetic Nanoparticles. *Adv. Funct. Mater.* **2022**, No. 2204732.
- (16) Derami, H. G.; Gupta, P.; Weng, K.-C.; Seth, A.; Gupta, R.; Silva, J. R.; Raman, B.; Singamaneni, S. Reversible Photothermal Modulation of Electrical Activity of Excitable Cells using Polydopamine Nanoparticles. *Adv. Mater.* **2021**, *33*, No. 2008809.
- (17) Marino, A.; Genchi, G. G.; Mattoli, V.; Ciofani, G. Piezoelectric nanotransducers: The future of neural stimulation. *Nano Today* **2017**, *14*, 9–12.
- (18) Maya-Vetencourt, J. F.; Manfredi, G.; Mete, M.; Colombo, E.; Bramini, M.; Di Marco, S.; Shmal, D.; Mantero, G.; Dipalo, M.; Rocchi, A.; DiFrancesco, M. L.; Papaleo, E. D.; Russo, A.; Barsotti, J.; Eleftheriou, C.; Di Maria, F.; Cossu, V.; Piazza, F.; Emionite, L.; Ticconi, F.; Marini, C.; Sambuceti, G.; Pertile, G.; Lanzani, G.; Benfenati, F. Subretinally injected semiconducting polymer nanoparticles rescue vision in a rat model of retinal dystrophy. *Nat. Nanotechnol.* **2020**, *15*, 698–708.
- (19) Singer, A.; Dutta, S.; Lewis, E.; Chen, Z.; Chen, J. C.; Verma, N.; Avants, B.; Feldman, A. K.; O'Malley, J.; Beierlein, M.; Kemere, C.; Robinson, J. T. Magnetoelectric Materials for Miniature, Wireless Neural Stimulation at Therapeutic Frequencies. *Neuron* **2020**, *107*, 631–643.e5.
- (20) Kozielski, K. L.; Jahanshahi, A.; Gilbert, H. B.; Yu, Y.; Erin, Ö.; Francisco, D.; Alosaimi, F.; Temel, Y.; Sitti, M. Nonresonant powering of injectable nanoelectrodes enables wireless deep brain stimulation in freely moving mice. *Sci. Adv.* **2021**, *7*, No. eabc4189.
- (21) Zeglio, E.; Rutz, A. L.; Winkler, T. E.; Malliaras, G. G.; Herland, A. Conjugated Polymers for Assessing and Controlling Biological Functions. *Adv. Mater.* **2019**, *31*, No. 1806712.
- (22) Shoda, S.-i.; Uyama, H.; Kadokawa, J.-i.; Kimura, S.; Kobayashi, S. Enzymes as Green Catalysts for Precision Macromolecular Synthesis. *Chem. Rev.* **2016**, *116*, 2307–2413.
- (23) Cruz-Silva, R.; Roman, P.; Romero, J. Enzymatic Synthesis of Polyaniline and Other Electrically Conductive Polymers. In *Biocatalysis in Polymer Chemistry*; Wiley-VCH, 2010; pp 187–210.
- (24) Romero-García, J.; Ledezma-Pérez, A.; Martínez-Cartagena, M.; Alvarado-Canché, C.; Jiménez-Cárdenas, P.; De-León, A.; Gallardo-Vega, C. Radical Addition Polymerization: Enzymatic Template-Free Synthesis of Conjugated Polymers and their Nanostructure Fabrication. In *Methods in Enzymology*, Bruns, N.; Loos, K., Eds.; Academic Press, 2019; pp 321–337.
- (25) K, N.; Rout, C. S. Conducting polymers: a comprehensive review on recent advances in synthesis, properties and applications. *RSC Adv.* **2021**, *11*, 5659–5697.
- (26) Povlich, L. K.; Cho, J. C.; Leach, M. K.; Corey, J. M.; Kim, J.; Martin, D. C. Synthesis, copolymerization and peptide-modification of

- carboxylic acid-functionalized 3,4-ethylenedioxythiophene (EDOTacid) for neural electrode interfaces. *Biochim. Biophys. Acta, Gen. Subj.* **2013**, *1830*, 4288–4293.
- (27) Ouyang, L.; Kuo, C.-c.; Farrell, B.; Pathak, S.; Wei, B.; Qu, J.; Martin, D. C. Poly[3,4-ethylene dioxythiophene (EDOT)-co-1,3,5-tri[2-(3,4-ethylene dioxythienyl)]-benzene (EPh)] copolymers (PEDOT-co-EPh): optical, electrochemical and mechanical properties. *J. Mater. Chem. B* **2015**, *3*, 5010–5020.
- (28) Wang, H.; Lin, J.; Shen, Z. X. Polyaniline (PANi) based electrode materials for energy storage and conversion. *J. Sci.: Adv. Mater. Devices* **2016**, *1*, 225–255.
- (29) Kulandaivalu, S.; Zainal, Z.; Sulaiman, Y. Influence of Monomer Concentration on the Morphologies and Electrochemical Properties of PEDOT, PANI, and PPy Prepared from Aqueous Solution. *Int. J. Polym. Sci.* **2016**, *2016*, *1*–12.
- (30) Nezakati, T.; Seifalian, A.; Tan, A.; Seifalian, A. M. Conductive Polymers: Opportunities and Challenges in Biomedical Applications. *Chem. Rev.* **2018**, *118*, *6766–6843*.
- (31) Martínez-Cartagena, M. E.; Bernal-Martínez, J.; Aranda-Sánchez, C. A.; Banda-Villanueva, A.; Gonzalez-Zapata, J. L.; Ledezma-Pérez, A.; Aguilar-Elguezabal, A.; Romero-García, J. Biomimetic Synthesized Conductive Copolymer EDOT-Pyrrole Electrodes for Electrocardiogram Recording in Humans. J. Mater. Sci. Chem. Eng. 2021, 9, 19–40.
- (32) Martínez-Cartagena, M. E.; Bernal-Martínez, J.; Banda-Villanueva, A.; Magaña, I.; Córdova, T.; Ledezma-Pérez, A.; Fernández-Tavizón, S.; de León, R. D. A Comparative Study of Biomimetic Synthesis of EDOT-Pyrrole and EDOT-Aniline Copolymers by Peroxidase-like Catalysts: Towards Tunable Semiconductive Organic Materials. Front. Chem. 2022, 10, No. 915264.
- (33) Haberberger, R. V.; Barry, C.; Matusica, D. Immortalized Dorsal Root Ganglion Neuron Cell Lines. *Front. Cell. Neurosci.* **2020**, *14*, No. 184
- (34) Banda-Villanueva, A.; González-Zapata, J. L.; Martínez-Cartagena, M. E.; Magaña, I.; Córdova, T.; López, R.; Valencia, L.; Medina, S. G.; Rodríguez, A. M.; Soriano, F.; de León, R. D. Synthesis and Vulcanization of Polymyrcene and Polyfarnesene Bio-Based Rubbers: Influence of the Chemical Structure over the Vulcanization Process and Mechanical Properties. *Polymers* **2022**, *14*, No. 1406.
- (35) Brar, A. S.; Goyal, A. K.; Hooda, S. Two-dimensional NMR studies of acrylate copolymers. *Pure Appl. Chem.* **2009**, *81*, 389–415.
- (36) Bai, R.; Yu, Y.; Wang, Q.; Yuan, J.; Fan, X. Laccase-mediated in situ polymerization of pyrrole for simultaneous coloration and conduction of wool fabric. *Text. Res. J.* **2018**, *88*, 27–35.
- (37) Bruno, F. F.; Fossey, S. A.; Nagarajan, S.; Nagarajan, R.; Kumar, J.; Samuelson, L. A. Biomimetic Synthesis of Water-Soluble Conducting Copolymers/Homopolymers of Pyrrole and 3,4-Ethylenedioxythiophene. *Biomacromolecules* **2006**, *7*, 586–589.
- (38) Santos, M. J. L.; Brolo, A. G.; Girotto, E. M. Study of polaron and bipolaron states in polypyrrole by in situ Raman spectroelectrochemistry. *Electrochim. Acta* **2007**, *52*, 6141–6145.
- (39) Kayser, L. V.; Lipomi, D. J. Stretchable Conductive Polymers and Composites Based on PEDOT and PEDOT:PSS. *Adv. Mater.* **2019**, *31*, No. 1806133.
- (40) Simon, P.; Taberna, P.-L.; Béguin, F. Electrical Double-Layer Capacitors and Carbons for EDLCs. In *Supercapacitors*; John Wiley & Sons, 2013; pp 131–165.
- (41) Kang, J.; Wen, J.; Jayaram, S. H.; Yu, A.; Wang, X. Development of an equivalent circuit model for electrochemical double layer capacitors (EDLCs) with distinct electrolytes. *Electrochim. Acta* **2014**, *115*, 587–598.
- (42) Leek, R.; Karunathilaka, S. A. G. R.; Hampson, N. A.; Sinclair, T. J. The Impedance of Small Li-CuO Primary Cells. In *Electrochemical Detectors: Fundamental Aspects and Analytical Applications*, Ryan, T. H., Ed.; Springer: Boston, MA, 1984; pp 149–164.
- (43) Stewart, K. C.; Kolman, D. G.; Taylor, S. R. The Effect of Parasitic Conduction Pathways on EIS Measurements in Low Conductivity Media. In *Electrochemical Impedance: Analysis and Interpretation*, Scully, J. R.; Silverman, D. C.; Kendig, M. W., Eds.; ASTM International: Fredericksburg, VA, 1993; pp 73–93.

- (44) Pyun, S.-I.; Shin, H.-C.; Lee, J.-W.; Go, J.-Y. Electrochemical Methods. In *Electrochemistry of Insertion Materials for Hydrogen and Lithium*, Springer: Berlin, Heidelberg, 2012; pp 11–32.
- (45) Moussa, M.; El-Kady, M. F.; Wang, H.; Michimore, A.; Zhou, Q.; Xu, J.; Majeswki, P.; Ma, J. High-performance supercapacitors using graphene/polyaniline composites deposited on kitchen sponge. *Nanotechnology* **2015**, *26*, No. 075702.
- (46) Mondal, S. K.; Barai, K.; Munichandraiah, N. High capacitance properties of polyaniline by electrochemical deposition on a porous carbon substrate. *Electrochim. Acta* **2007**, *52*, 3258–3264.
- (47) Gopalakrishnan, K.; Sultan, S.; Govindaraj, A.; Rao, C. N. R. Supercapacitors based on composites of PANI with nanosheets of nitrogen-doped RGO, BC1.5N, MoS2 and WS2. *Nano Energy* **2015**, *12*, 52–58.
- (48) Brownson, D. A. C.; Banks, C. E. Interpreting Electrochemistry. In *The Handbook of Graphene Electrochemistry*, Springer: London, 2014; pp 23–77.
- (49) Zhao, D.; Jiang, K.; Li, J.; Zhu, X.; Ke, C.; Han, S.; Kymakis, E.; Zhuang, X. Supercapacitors with alternating current line-filtering performance. *BMC Mater.* **2020**, 2, No. 3.
- (50) Flynn, K. C. The cytoskeleton and neurite initiation. *Bioarchitecture* **2013**, *3*, 86–109.
- (51) Jeon, K.-I.; Huxlin, K. R. How scars shape the neural landscape: Key molecular mediators of TGF- β 1's anti-neuritogenic effects. *PLoS One* **2020**, *15*, No. e0234950.
- (52) Nichols, E. L.; Green, L. A.; Smith, C. J. Ensheathing cells utilize dynamic tiling of neuronal somas in development and injury as early as neuronal differentiation. *Neural Dev.* **2018**, *13*, No. 19.
- (53) Burnstine-Townley, A.; Eshel, Y.; Amdursky, N. Conductive Scaffolds for Cardiac and Neuronal Tissue Engineering: Governing Factors and Mechanisms. *Adv. Funct. Mater.* **2020**, *30*, No. 1901369.
- (54) Farokhi, M.; Mottaghitalab, F.; Saeb, M. R.; Shojaei, S.; Zarrin, N. K.; Thomas, S.; Ramakrishna, S. Conductive Biomaterials as Substrates for Neural Stem Cells Differentiation towards Neuronal Lineage Cells. *Macromol. Biosci.* **2021**, 21, No. 2000123.
- (55) Colombo, E.; Feyen, P.; Antognazza, M. R.; Lanzani, G.; Benfenati, F. Nanoparticles: A Challenging Vehicle for Neural Stimulation. *Front. Neurosci.* **2016**, *10*, No. 105.
- (56) Rocha, I.; Cerqueira, G.; Penteado, F. V.; de Torresi, S. I. C. Electrical Stimulation and Conductive Polymers as a Powerful Toolbox for Tailoring Cell Behaviour in vitro. *Front. Med. Technol.* **2021**, 3, No. 670274.
- (57) Richardson-Burns, S. M.; Hendricks, J. L.; Foster, B.; Povlich, L. K.; Kim, D.-H.; Martin, D. C. Polymerization of the conducting polymer poly(3,4-ethylenedioxythiophene) (PEDOT) around living neural cells. *Biomaterials* **2007**, 28, 1539–1552.
- (58) Chen, H.-l.; Yang, D.; Chen, C.-r.; Tian, G.-z.; Kim, D.-H. In situ polymerization of conducting polymers around living neural cells: Cellular effect study. *Colloids Surf., B* **2022**, *213*, No. 112410.
- (59) Kim, H. J.; Lee, J. S.; Park, J. M.; Lee, S.; Hong, S. J.; Park, J. S.; Park, K.-H. Fabrication of Nanocomposites Complexed with Gold Nanoparticles on Polyaniline and Application to Their Nerve Regeneration. ACS Appl. Mater. Interfaces 2020, 12, 30750–30760.
- (60) Michelson, N. J.; Eles, J. R.; Vazquez, A. L.; Ludwig, K. A.; Kozai, T. D. Y. Calcium activation of cortical neurons by continuous electrical stimulation: Frequency dependence, temporal fidelity, and activation density. *J. Neurosci. Res.* **2019**, *97*, 620–638.
- (61) Mi, J.; Xu, J.-K.; Yao, Z.; Yao, H.; Li, Y.; He, X.; Dai, B.-Y.; Zou, L.; Tong, W.-X.; Zhang, X.-T.; Hu, P.-J.; Ruan, Y. C.; Tang, N.; Guo, X.; Zhao, J.; He, J.-F.; Qin, L. Implantable Electrical Stimulation at Dorsal Root Ganglions Accelerates Osteoporotic Fracture Healing via Calcitonin Gene-Related Peptide. *Adv. Sci.* 2022, *9*, No. 2103005.
- (62) Borrachero-Conejo, A. I.; Saracino, E.; Natali, M.; Prescimone, F.; Karges, S.; Bonetti, S.; Nicchia, G. P.; Formaggio, F.; Caprini, M.; Zamboni, R.; Mercuri, F.; Toffanin, S.; Muccini, M.; Benfenati, V. Electrical Stimulation by an Organic Transistor Architecture Induces Calcium Signaling in Nonexcitable Brain Cells. *Adv. Healthcare Mater.* **2019**, *8*, No. 1801139.

- (63) Schiefer, M. A.; Grill, W. M. Sites of neuronal excitation by epiretinal electrical stimulation. *IEEE Trans. Neural Syst. Rehabil. Eng.* **2006**, *14*, 5–13.
- (64) McCreery, D. B.; Agnew, W. F.; Yuen, T. G. H.; Bullara, L. A. Comparison of neural damage induced by electrical stimulation with faradaic and capacitor electrodes. *Ann. Biomed. Eng.* **1988**, *16*, 463–481.
- (65) Günter, C.; Delbeke, J.; Ortiz-Catalan, M. Safety of long-term electrical peripheral nerve stimulation: review of the state of the art. *J. NeuroEng. Rehabil.* **2019**, *16*, No. 13.
- (66) Reviakine, I.; Johannsmann, D.; Richter, R. P. Hearing What You Cannot See and Visualizing What You Hear: Interpreting Quartz Crystal Microbalance Data from Solvated Interfaces. *Anal. Chem.* **2011**, 83, 8838–8848.
- (67) Easley, A. D.; Ma, T.; Eneh, C. I.; Yun, J.; Thakur, R. M.; Lutkenhaus, J. L. A practical guide to quartz crystal microbalance with dissipation monitoring of thin polymer films. *J. Polym. Sci.* **2022**, *60*, 1090–1107.
- (68) Leppin, C.; Langhoff, A.; Poggemann, H.-F.; Gödde, A. S.; Johannsmann, D. Fast and slow EQCM response of zwitterionic weak electrolytes to changes in the electrode potential: a pH-mediated mechanism. *Analyst* **2021**, *146*, 6005–6013.
- (69) Carton, I.; Brisson, A. R.; Richter, R. P. Label-Free Detection of Clustering of Membrane-Bound Proteins. *Anal. Chem.* **2010**, 82, 9275–9281
- (70) Nunez, J. Primary Culture of Hippocampal Neurons from P0 Newborn Rats. J. Visualized Exp. 2008, No. e895.
- (71) Pacifici, M.; Peruzzi, F. Isolation and Culture of Rat Embryonic Neural Cells: A Quick Protocol. *J. Visualized Exp.* **2012**, No. e3965.